

Distorted Black Hole Initial Data Using the Puncture Method

J. David Brown and Lisa L. Lowe

Department of Physics, North Carolina State University, Raleigh, NC 27695 USA

We solve for single distorted black hole initial data using the puncture method, where the Hamiltonian constraint is written as an elliptic equation in \mathbf{R}^3 for the nonsingular part of the metric conformal factor. With this approach we can generate isometric and non-isometric black hole data. For the isometric case, our data are directly comparable to those obtained by Bernstein *et al.*, who impose isometry boundary conditions at the black hole throat. Our numerical simulations are performed using a parallel multigrid elliptic equation solver with adaptive mesh refinement. Mesh refinement allows us to use high resolution around the black hole while keeping the grid boundaries far away in the asymptotic region.

I. INTRODUCTION

Distorted black holes are expected to be produced by astrophysical events such as asymmetrical gravitational collapse, black hole–black hole coalescence, black hole–neutron star coalescence, and possibly neutron star–neutron star coalescence. As ground based gravitational wave detectors such as LIGO, VIRGO, TAMA, and GEO increase their sensitivities, and the planned launch date for the space based detector LISA grows near, the need for researchers to develop a theoretical understanding of these systems becomes increasingly important. In support of that effort, we need to develop the techniques and tools to evolve a dynamic, distorted black hole and extract the emitted gravitational radiation as it settles to a quiescent state.

One of the difficulties encountered in the numerical treatment of single and multiple black hole systems is the presence of nontrivial topologies. In the past, researchers have addressed this problem by using isometry conditions at inner boundaries to represent black hole throats. Another approach to black hole evolution is excision, in which a region inside each apparent horizon is removed from the computational domain. Recently it has been shown that black holes can be treated in terms of fields on \mathbf{R}^3 by splitting the conformal factor for the spatial metric into singular and non-singular terms. This so-called “puncture method” was applied to the Bowen–York [1] family of black hole initial data sets by Brandt and Brügmann [2], and used for evolution studies by Brügmann [3] and others (see, for example, Refs. [4, 5]).

In this paper we make a modest extension of the puncture construction for initial data to include single distorted black holes. We reproduce and extend the results of Bernstein *et al.* [6, 7, 8], who constructed “black hole plus Brill wave” initial data sets using isometry conditions at the black hole throat. Whereas the black holes obtained by Bernstein *et al.* are isometric by construction, our distorted puncture black hole data sets are isometric only when the free parameters μ and m , defined in Sec. II, are equal to one another. For $\mu \neq m$, we obtain non-isometric, distorted black holes.

Another difficulty encountered in the numerical modeling of black holes is the wide discrepancy in length

scales involved. The computational grid needs to be large enough to capture outgoing gravitational waves and to minimize boundary effects. The grid must also have high resolution in the interior to accurately resolve the strong gravitational fields of black holes. For a finite difference code, adaptive mesh refinement (AMR) is needed to satisfy both of these requirements: high resolution and a large grid. In this paper we introduce our AMR elliptic solver that allows us to solve accurately for puncture black hole data on very large grids. Evolution studies of these data sets are underway [9].

In Sec. II we set up the equations defining the initial value problem for a distorted puncture black hole. We show how the puncture data can be formulated to give isometric data sets, thus enabling a comparison with the results of Bernstein *et al.* In Sec. III we give a brief description of our AMR elliptic solver. In Sec. IV we present sample results both for isometric and non-isometric black hole data.

II. FORMULATION OF THE PROBLEM

Following Bernstein *et al.* [6, 7, 8] we write the line element for the physical metric g_{ij} as

$$ds^2 = \psi^4 [e^{2q}(dr^2 + r^2 d\theta^2) + r^2 \sin^2 \theta d\phi^2], \quad (1)$$

where q is a specified function of the spatial coordinates and ψ is the conformal factor. In this paper we restrict ourselves to the expression for q used in Ref. [7], namely,

$$q(r, \theta, \phi) = 2Q_0 e^{-\eta^2} \sin^n \theta (1 + c \cos^2 \phi), \quad (2)$$

where $\eta = \ln(2r/\mu)$. In Eq. (2), Q_0 , n , c and μ are adjustable constants that affect the size and type of distortion. We also restrict ourselves to data sets defined at a moment of time symmetry. Thus, the extrinsic curvature vanishes and the momentum constraints are trivially satisfied. The Hamiltonian constraint reduces to

$$\hat{\nabla}^2 \psi - \frac{1}{8} \hat{R} \psi = 0, \quad (3)$$

where $\hat{\nabla}^2$ and \hat{R} are the Laplacian and scalar curvature of the conformal metric, defined by $\hat{g}_{ij} = \psi^{-4} g_{ij}$.

Solutions of Eq. (3) on the manifold \mathcal{R}^3 are Brill waves. The distorted black hole data sets of Bernstein *et al.* were obtained by solving Eq. (3) on the manifold $\mathcal{R} \times S^2$, with Robin conditions at the outer boundary [$\partial(r\psi-r)/\partial r = 0$ as $r \rightarrow \infty$] and isometry conditions at the inner boundary [$\partial(\sqrt{r}\psi)/\partial r = 0$ at $r = \mu/2$]. We will obtain solutions of Eq. (3) on $\mathcal{R} \times S^2$ by following the puncture construction of Ref. [2]. Thus, we write the conformal factor as $\psi = u + m/(2r)$ and insert this into the Hamiltonian constraint (3) to obtain

$$\hat{\nabla}^2 u - \frac{1}{8} \hat{R} u = \frac{m}{16r} \hat{R}. \quad (4)$$

This equation is solved for a continuous solution u on \mathcal{R}^3 with Robin boundary conditions $\partial(ru - r)/\partial r = 0$ at $r \rightarrow \infty$. Note that the “bare mass” m appears as a new parameter in the construction.¹

We have had no difficulty in obtaining numerical solutions to Eq. (4). However, from an analytical point of view, it is not immediately obvious to us whether or not Eq. (4) always admits solutions, and if so whether those solutions are unique. The problem of existence and uniqueness of solutions of Eq. (4) on \mathcal{R}^3 is similar to the problem of existence and uniqueness of solutions of Eq. (3) on \mathcal{R}^3 . There are two notable differences. First is the appearance of a “source” term $m\hat{R}/(16r)$ on the right-hand side of Eq. (4). Note that with the choice (2) for the function q , the scalar curvature \hat{R} goes to zero rapidly, $\hat{R} \sim (\ln(r))^2 r^{\ln(\mu/r) - 2 - 2\ln(2)}$ at $r \rightarrow 0$, so that \hat{R}/r does not blow up at the puncture. The second difference between equation (4) and the familiar initial value equation (3) is that, for (4), we need not require the solutions to be positive. Rather, we would like to know if u is greater than $-m/(2r)$ so that the combination $\psi = u + m/(2r)$ is everywhere positive.

By construction the data sets of Bernstein *et al.* are isometric; that is, they are symmetric under reflections about the black hole throat $r = \mu/2$. More precisely, each data set is described by a metric tensor whose components g_{ij} , as functions of r , θ and ϕ , are unchanged by the coordinate transformation $r \rightarrow \bar{r} \equiv \mu^2/(4r)$. We can solve for reflection symmetric data sets using the puncture method as well, simply by setting the parameters μ and m equal to one another: $\mu = m$. To see this, we first note that the Hamiltonian constraint on $\mathcal{R} \times S^2$ can be written as (see, for example, Appendix D of Ref. [10])

$$\left(\tilde{\nabla}^2 - \frac{1}{8} \tilde{R} \right) (\sqrt{r}\psi) = 0, \quad (5)$$

where $\tilde{\nabla}^2$ and \tilde{R} are the Laplacian and scalar curvature for the metric $\tilde{g}_{ij} = \hat{g}_{ij}/r^2$. Let $\psi_1(r)$ denote a solution

of Eq. (3), or equivalently Eq. (5), obtained by the puncture method. (For notational simplicity, we display only the r dependence in the solution ψ_1 , and in ψ_2 below. In general these are functions of θ and ϕ as well.) This solution $\psi_1(r)$ has boundary behavior $\psi_1(r) \rightarrow 1$ as $r \rightarrow \infty$, and $\psi_1(r) \rightarrow m/(2r)$ as $r \rightarrow 0$. Now observe that the line element $ds^2 = \tilde{g}_{ij} dx^i dx^j$, with the function q chosen as in Eq. (2), is invariant under reflections $r \rightarrow \bar{r} = \mu^2/(4r)$. The scalar operator $\tilde{\nabla}^2 - \tilde{R}/8$ is invariant as well. By making the substitution $r \rightarrow \bar{r} = \mu^2/(4r)$ in Eq. (5) we see that $\psi_2(r)$, defined by $\sqrt{r}\psi_2(r) = \sqrt{\bar{r}}\psi_1(\bar{r})$ with $\bar{r} = \mu^2/(4r)$, is also a solution of Eqs. (5) and (3). This solution satisfies the boundary conditions $\psi_2(r) \rightarrow m/\mu$ as $r \rightarrow \infty$ and $\psi_2(r) \rightarrow \mu/(2r)$ as $r \rightarrow 0$. If we choose $\mu = m$, then the solutions $\psi_1(r)$ and $\psi_2(r)$ satisfy the same equation and obey the same boundary conditions. If we assume that solutions to the puncture equation (4) are unique, then the two solutions $\psi_1(r)$ and $\psi_2(r)$ must in fact be identical. From the equality $\psi_1(r) = \psi_2(r)$ we find

$$\sqrt{r}\psi_1(r) = \left(\sqrt{\bar{r}}\psi_1(\bar{r}) \right) \Big|_{\bar{r}=\mu^2/(4r)}. \quad (6)$$

The line element (1) for this solution can be written as

$$ds^2 = (\sqrt{r}\psi_1(r))^4 [e^{2q}(dr^2/r^2 + d\theta^2) + \sin^2 \theta d\phi^2]. \quad (7)$$

Then the relation (6) is the condition for the physical metric (7) to be invariant under the reflection $r \rightarrow \bar{r} = \mu/(4r)$.

In Sec. IV we present results for the conformal factor ψ for isometric ($\mu = m$) and non-isometric ($\mu \neq m$) data sets. For isometric data, we can check the reflection symmetry by comparing the ADM mass computed at the two infinities. At the “outer” infinity ($r \rightarrow \infty$) the ADM mass is given by [11]

$$M_\infty = -\frac{1}{2\pi} \oint_\infty d\hat{S}^i \hat{\nabla}_i \psi. \quad (8)$$

Numerically, the integral is computed at the outer boundary of the computational domain. The ADM mass at the “inner” infinity ($r = 0$) is found by expressing the metric (1) in coordinates \bar{r} , θ , ϕ , where $\bar{r} = m^2/(4r)$. We find

$$ds^2 = \left(1 + \frac{mu}{2\bar{r}} \right)^4 [e^{2q}(d\bar{r}^2 + \bar{r}^2 d\theta^2) + \bar{r}^2 \sin^2 \theta d\phi^2], \quad (9)$$

where q and u are functions of $r = m^2/(4\bar{r})$, θ , and ϕ . Provided q goes to zero sufficiently rapidly as $\bar{r} \rightarrow \infty$, the metric is asymptotically flat at $r = 0$ with ADM mass given by

$$M_0 = m u|_{r=0}. \quad (10)$$

The choice (2) for q vanishes as $r \rightarrow 0$ like $q \sim r^{\ln(\mu/r)}$, faster than any power of r .

¹ The parameters μ and m are dimensionful. Thus, our data sets can be described in terms of the dimensionless parameters c , Q_0 , n , the dimensionless ratio μ/m , and the dimensionless coordinates x/m , y/m , and z/m .

III. NUMERICAL CODE

Our numerical code solves Eq. (4) using multigrid techniques with mesh refinement. We use the Paramesh package [12, 13] to implement mesh refinement and parallelization. Paramesh divides the computational grid into blocks, with each block containing N zones. A block of data is refined by bisection—that is, the block is divided into eight “child” blocks (in three spatial dimensions) each containing N zones.

Our code carries out multigrid V-cycles using the Full Approximation Storage (FAS) algorithm [14] on non-uniform grid structures, with zone-centered data. It works with both fixed mesh refinement (FMR) and adaptive mesh refinement (AMR). Working with FMR, we specify a non-uniform grid by hand. The code V-cycles until the L_2 norm of the residual across the computational domain is smaller than the L_2 norm of the relative truncation error. Working with AMR, we generally start with a coarse, uniform grid. The code V-cycles until the norm of the residual is less than the norm of the relative truncation error, then computes the norm of the relative truncation error for each block. Any block whose relative truncation error is above a specified tolerance is flagged for refinement. Paramesh then rebuilds the grid, the data is prolonged from the old grid to the new, and the V-cycle process begins again. Working in this mode takes the place of the Full Multigrid (nested iteration) Algorithm [14], where the solution on the final grid structure is reached by a succession of V-cycles of increasing peak resolution.

We will provide details of the AMR-multigrid algorithm in a later publication, along with numerous code tests.

IV. RESULTS

Bernstein *et al.* [6, 7, 8] produced nonaxisymmetric distorted black holes using isometry conditions at the black hole throat. We have reproduced several of the initial data sets from Ref. [7] using the puncture method, by setting $\mu = m$ as described in Sec. II. Our values for the ADM masses at infinity agree with theirs. As a check for isometry, we have confirmed that the ADM mass at the puncture, M_0 , agrees with the ADM mass at infinity, M_∞ , to several significant digits.

As a specific example let us consider the data set discussed in Ref. [7] with $c = -2$, $Q_0 = -0.5$, $n = 4$, and $\mu = m = 2$. The ADM masses for this data at infinity and at the puncture are $M_\infty = 2.2021$ and $M_0 = 2.2027$. Figure 1 shows a contour plot of the nonsingular part u of the conformal factor in the $z = 0$ plane. The contour levels crossing the x axis between -100 and zero are, respectively, $\{1.0015, 1.005, 1.005, 1.0015, 0.96\}$. The contour levels crossing the y axis between -100 and zero are, respectively, $\{1.0015, 1.005, 1.01, 1.02, 1.1\}$. The inset in Fig. 1 shows the range in x and y from -13 to 13 . In the

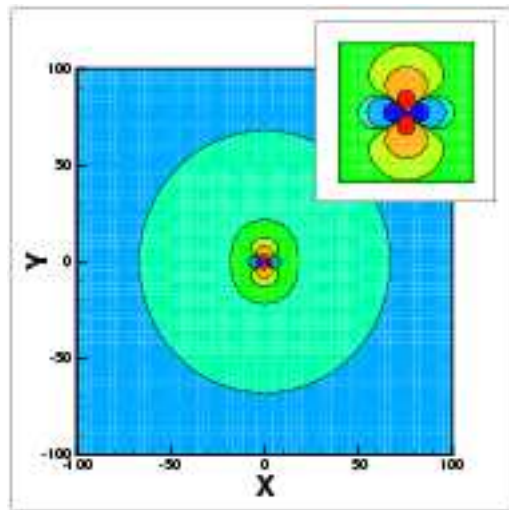


FIG. 1: Contour plot of u in the $z = 0$ plane for the case $c = -2$, $Q_0 = -0.5$, $n = 4$, $\mu = m = 2$. The full AMR grid extends from -100 to 100 , while the inset shows the range -13 to 13 .

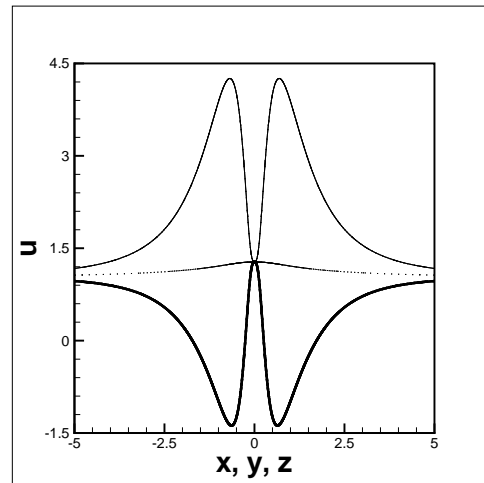


FIG. 2: The function u plotted along the three coordinate axes for a non-isometric distorted black hole with $c = -2$, $Q_0 = -0.5$, $n = 4$, $\mu = 2$, $m = 10$. The thin solid line (top curve) is u along the y -axis, the dotted line (middle curve) is u along the z -axis, and the thick solid line (bottom curve) is u along the x -axis.

inset figure, the contours crossing the x axis between -13 to zero are $\{1.005, 1.0015, 0.96\}$ and the contours crossing the y axis between -13 and zero are $\{1.01, 1.02, 1.1\}$. The function u forms two peaks along the y axis with maximum values 2.03 , and two valleys along the x axis with minimum values 0.296 . The value of u at the puncture is 1.10 . The profiles of u along the three axes look similar to those shown in Fig. 2.

With AMR, we are able to push the boundaries out quite far while maintaining high resolution around the puncture. For the data described above, the computa-

tional grid extends from -100 to 100 and has refined itself to reach a maximum relative truncation error of 0.005 . The lowest resolution region is equivalent to a 64^3 grid with $\Delta x = 3.125$. The highest resolution region is equivalent to a $262,144^3$ grid with $\Delta x = 0.000763$.

The puncture method allows us to define a new class of initial data: distorted black holes that are not isometric ($\mu \neq m$). Figure 2 shows such a data set with $c = -2$, $Q_0 = -0.5$, $n = 4$, $\mu = 2$, and $m = 10$. The results were computed on a grid extending from -100 to 100 in each dimension. The grid spacing for the lowest resolution region, adjacent to the grid boundaries, is $\Delta x = 3.125$. The grid spacing for the highest resolution region, surrounding the puncture, is $\Delta x = 0.01221$. The ADM mass at infinity is $M_\infty = 10.7$, while the ADM mass at the puncture is $M_0 = 12.8$. Figure 2 shows the behavior of the nonsingular part u of the conformal factor along the coordinate axes. The thin solid line plots u along the y axis, the thick solid line plots u along the x axis, and the dotted line plots u along the z axis. The two peaks in u along the y -axis have maximum values 4.26 , and the two valleys along the x -axis have minimum values -1.38 . The value of u at the puncture is 1.28 .

Note that for the non-isometric data described above, u takes on negative values in two small regions of radius ~ 1 at locations $\sim \pm 1$ along the x axis. However, for this

data set, the conformal factor $\psi = u + m/(2r)$ is everywhere positive. We have explored other data sets that contain regions with $u < 0$, and in each case we find that the conformal factor ψ is positive everywhere. For data with $c = -2$, $Q_0 = -0.5$, and $n = 4$, the most extreme data sets we have studied have ratios $\mu/m = 1/300$ and $\mu/m = 100$. For the case $\mu/m = 1/300$, the function u reaches a minimum value of ~ -120 but the conformal factor remains positive. For the case $\mu/m = 100$ the function u , and therefore also ψ , is always positive.

Acknowledgments

We would like to thank the numerical relativity group at NASA Goddard Space Flight Center, and especially Dae-Il Choi, for their help and support. We would also like to thank James Isenberg, Kevin Olson, and Peter MacNeice for helpful discussions. This work was supported by NASA Space Sciences Grant ATP02-0043-0056. Computations were carried out on the North Carolina State University IBM Blade Center Linux Cluster. The PARAMESH software used in this work was developed at NASA Goddard Space Flight Center under the HPC and ESTO/CT projects.

-
- [1] J. M. Bowen and J. York, James W., Phys. Rev. **D21**, 2047 (1980).
 - [2] S. Brandt and B. Brugmann, Phys. Rev. Lett. **78**, 3606 (1997), gr-qc/9703066.
 - [3] B. Brugmann, Int. J. Mod. Phys. **D8**, 85 (1999), gr-qc/9708035.
 - [4] M. Alcubierre et al., Phys. Rev. **D67**, 084023 (2003), gr-qc/0206072.
 - [5] B. Imbiriba, J. Baker, D.-I. Choi, J. Centrella, D. R. Fiske, J. D. Brown, J. R. van Meter, and K. Olson, (gr-qc/0403048) (2004).
 - [6] D. Bernstein, D. Hobill, E. Seidel, and L. Smarr, Phys. Rev. **D50**, 3760 (1994).
 - [7] S. Brandt, K. Camarda, E. Seidel, and R. Takahashi, Class. Quant. Grav. **20**, 1 (2003), gr-qc/0206070.
 - [8] S. R. Brandt and E. Seidel, Phys. Rev. **D54**, 1403 (1996), gr-qc/9601010.
 - [9] D. R. Fiske *et al.*, work in progress.
 - [10] R. M. Wald, *General Relativity* (University of Chicago Press, Chicago, 1984).
 - [11] N. Ó Murchadha and J. W. York, Phys. Rev. **10**, 2345 (1974).
 - [12] http://ct.gsfc.nasa.gov/paramesh/Users_manual/amr.html.
 - [13] P. MacNeice, K. M. Olson, C. Mobarry, R. deFainchtein, and C. Packer, Computer Physics Comm. **126**, 330 (2000).
 - [14] W. H. Press, S. A. Teukolsky, W. T. Vetterling, and B. P. Flannery, *Numerical Recipes* (Cambridge University Press, Cambridge, 1992).